Vacancy-Driven Noncubic Local Structure and Magnetic Anisotropy Tailoring in Fe_xO-$Fe_{3-\delta}O_4$ Nanocrystals

Alexandros Lappas[1,*], George Antonaropoulos,[1,2] Konstantinos Brintakis,[1] Marianna Vasilakaki,[3] Kalliopi N. Trohidou,[3] Vincenzo Iannotti,[4] Giovanni Ausanio,[4] Athanasia Kostopoulou,[1] Milinda Abeykoon,[5] Ian K. Robinson,[6,7] and Emil S. Bozin[6]

[1]*Institute of Electronic Structure and Laser, Foundation for Research and Technology-Hellas, Vassilika Vouton, 71110 Heraklion, Greece*
[2]*Department of Chemistry, University of Crete, Voutes, 71003 Heraklion, Greece*
[3]*Institute of Nanoscience and Nanotechnology, National Center for Scientific Research Demokritos, 15310 Athens, Greece*
[4]*CNR-SPIN and Department of Physics E. Pancini, University of Naples Federico II, Piazzale V. Tecchio 80, 80125 Naples, Italy*
[5]*Photon Sciences Division, National Synchrotron Light Source II, Brookhaven National Laboratory, Upton, New York 11973, USA*
[6]*Condensed Matter Physics and Materials Science Department, Brookhaven National Laboratory, Upton, New York 11973, USA*
[7]*London Centre for Nanotechnology, University College, London WC1E 6BT, United Kingdom*

In contrast to bulk materials, nanoscale crystal growth is critically influenced by size- and shape-dependent properties. However, it is challenging to decipher how stoichiometry, in the realm of mixed-valence elements, can act to control physical properties, especially when complex bonding is implicated by short- and long-range ordering of structural defects. Here, solution-grown iron-oxide nanocrystals (NCs) of the pilot wüstite system are found to convert into iron-deficient rock-salt and ferro-spinel subdomains but attain a surprising tetragonally distorted local structure. Cationic vacancies within chemically uniform NCs are portrayed as the parameter to tweak the underlying properties. These lattice imperfections are shown to produce local exchange-anisotropy fields that reinforce the nanoparticles' magnetization and overcome the influence of finite-size effects. The concept of atomic-scale defect control in subcritical-size NCs aspires to become a pathway to tailor-made properties with improved performance for hyperthermia heating over defect-free NCs.

Subject Areas: Condensed Matter Physics, Magnetism, Nanophysics

I. INTRODUCTION

Iron oxides are at the research forefront as they encompass important mixed-valent states [1] that impact their physical properties and their technological potential [2], extending from energy storage devices to catalysts and electrochemical cells. Moreover, since the principal oxidation states (II-IV) of iron carry atomic magnetic moments, spontaneous cooperative magnetic order is stabilized, which offers a highly exploitable modality, extending from spintronics and recording media [3] to the rapidly developing field of nanobiotechnology [4]. In the latter field of interest, nanoscale magnetic particles for biomedical applications draw significant benefits from the volume dependence of magnetism, especially when superparamagnetism (a state not permanently magnetized) is established below a critical particle size [5]. Consequently, there is high demand for controlling the crossover amongst different states of magnetization in order to improve the particle's magnet-facilitated performance, for making image contrast agents, heat emission "hyperthermia" systems, or even mechanical-force nanovectors [6].

More specifically, radio-frequency magnetic heating of single-crystalline nanoparticles [i.e., nanocrystals (NCs)] is emerging as a novel strategy for activating temperature-sensitive cellular processes [7], but it requires nontoxic biocompatible nanomaterials and an understanding of how structure-morphology relationships can be used as design

---

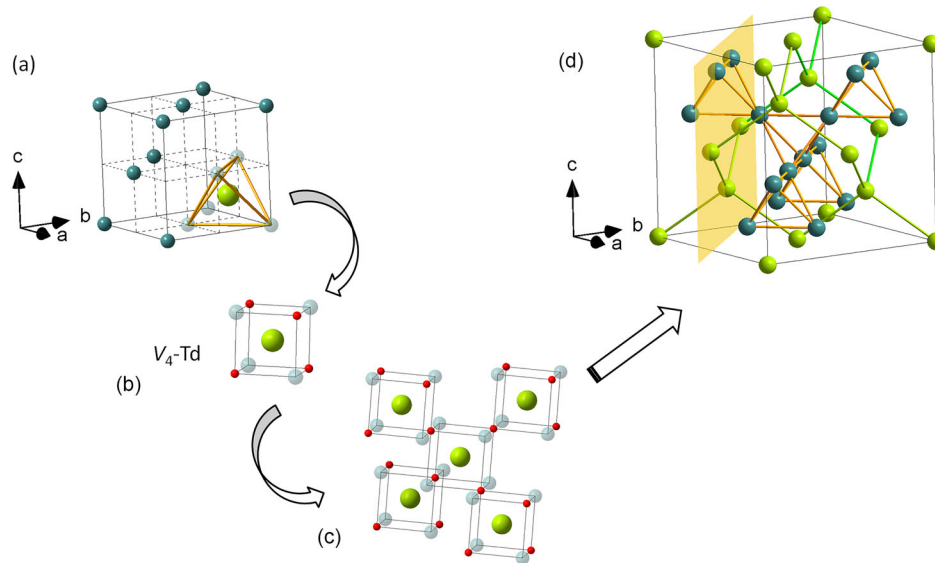[*]Corresponding author.
lappas@iesl.forth.gr

FIG. 1.   Illustrations of the Fe-site arrangement in archetype face-centered cubic crystal types of bulk iron oxides, namely, wüstite (Fe_xO) (a), a defect-mediated rock-salt structure, with octahedrally coordinated (by oxygen–not shown for clarity) ferrous (Fe^{2+}) sites (Oh; represented by dark green spheres), and interstitial ferric (Fe^{3+}) tetrahedral sites (Td; depicted by large light green spheres) in the presence of four vacant (V) iron positions (light green). Such units compose $V_4 - Td$ defect clusters (b) (oxygen shown by red spheres), whose coalescence (c) [28] offers a likely pathway towards the nucleation of $Fe_{3-\delta}O_4$ (magnetite) (d). The latter represents the ferrospinel family, with Fe atoms in both types of coordination environment, and vacancy-bearing (220) lattice planes (highlighted). Both structural types accommodate trigonal pyramids of Fe atoms as a common building block, forming a pyrochlore-type sublattice in magnetite.

parameters. Optimizing hyperthermia efficacy depends on magnetic loss mechanisms attributed to Néel-Brown relaxations, which evolve with the magnetic anisotropy constant (K) and saturation magnetization (M_S) [8]. In practice, relaxation times vary by changing intrinsic nanocrystal factors, including size [9], shape [10], and composition [11]. While single magnetic cores of pure iron-metal particles may offer superior heating efficiency, their questionable stability in biological media [12] has led researchers to develop iron-oxide particles (e.g., ferrites: $Fe_{3-\delta}O_4$, $\gamma - Fe_2O_3$, etc.) as a versatile and biocompatible class of materials [13].

The quest for NCs that surpass the performance of a single magnetic core is motivated further by the design concept of controlling the spatial distribution of chemical composition within a single motif [14] such as core@shell and thin-film heterostructures. Distinct phases grown in a core@shell topology, with contrasting magnetic-state constituents [e.g., antiferromagnetic (AFM), ferromagnetic (FM) and/or ferrimagnetic (FiM) subdomains], offer a powerful way to tune the nanoscale magnetic properties and boost the particle's hyperthermia response [10]. This case rests on the important capability to adjust the particle's anisotropy through the interfacial exchange interactions between the bimagnetic component phases [15]. The extent to which the emerging exchange bias (H_{EB}) [16] plays a key role is regulated by varying the core-shell volume ratio, the surface or interface structure, and the composition itself [17]. Thus, optimal design of hyperthermia agents requires

the right kind of defect structure to modulate favorable magnetic relaxations. As we show in this work, these mechanisms can be modeled using Monte Carlo methods.

In this endeavor, solution-chemistry methods are widely used to develop size-controlled [18] and shape-controlled [19] ferrite-based nanocrystals and to facilitate their interfacial connectivity on a nanoscale motif, e.g., $Fe@Fe_{3-\delta}O_4$ [20], $CoO@CoFe_2O_4$ [21], $FePt@MFe_2O_4$ ($M = Mn$, Fe, Co, Zn) [22], etc. Within these systems, unforeseen magnetic properties are occasionally reported [23–26], especially when thermodynamically metastable phases such as wüstite [27] or novel interfaces are introduced during the nanoscale particle nucleation and growth. For example, during the oxidative conversion of AFM wüstite [Fe_xO, Fig. 1(a)], invoking clustering of interstitials and vacancies [Figs. 1(b) and 1(c)] [28] into a FiM spinel magnetite [$Fe_{3-\delta}O_4$, Fig. 1(d)], the internal structure of the as-made core@shell $Fe_xO@Fe_3O_4$ NCs evolves with the composition gradients influenced by stresses [29]. While a reduction in the AFM@FM interface area and core anisotropy lowers H_{EB} [30], antiphase boundaries (APBs) in the structure are found to raise the particle anisotropy. Surprisingly, this paves the way to nonzero H_{EB} even in the fully oxidized, $Fe_{3-\delta}O_4$-like derivatives of wüstite [25]. It is interesting to note that APB defects are a favored low-energy growth pathway for Fe_3O_4-films [31] that modify the exchange interactions and give rise to anomalous magnetic behavior with important applications [32,33]. These peculiar performances, for NCs in the

critical-size range of 20–30 nm, were correlated with perturbations of the periodic potential of the iron atomic coordination by lattice defects, which are hard to waive out in post synthesis treatments but are preventable by strategic redox tuning of the Fe valence during the reaction itself [34].

The preceding discussion demonstrates that the properties of otherwise single-crystalline ferrite particles are influenced by a significant fraction of atoms at the various particle "limits," the surfaces and internal interfaces [35–37]. This case necessitates characterization of the detailed atomic arrangements within the $Fe_xO - Fe_3O_4$ phase space available to the chemical synthesis methods. Effectively, research efforts focus on solving a multiple-length-scale problem [38] by combining surface (e.g., electron microscopy) and bulk (e.g., powder diffraction) sensitive probes. Total scattering experiments, though, coupled to atomic pair distribution function (PDF) analysis can reach beyond such limitations [39]. Our present work reports on the added value of the PDF method, which, in contrast to near-neighbor probes like EXAFS and NMR, is able to probe a relatively wide field of view (about 10 nm) in a single experiment by reporting how local (nanoscale) distortions are correlated throughout the structure.

While chemical phase and stoichiometry ultimately control nanoscale magnetic properties, the rational choice of the critical particle size, with optimal magnetic anisotropy [40], is about 20 nm, and it determines the applications [39,41]. In practice though, thermodynamic and kinetic parameters at nanoscale surfaces and interfaces are expected to trigger nanoscale crystal growth via energetically favorable structural-defect pathways. This process serves to render the control of defects as an extra tuning knob. Here, we investigate the nature of structural defects established during the course of the spontaneous, oxidative conversion of wüstite into $Fe_xO - Fe_3O_4$ NCs. We focus on a series of NCs with increasing particle size in the range 8–18 nm, which differ structurally and morphologically. Our results establish a quantitative relationship between favorable vacancy-induced disorder and tailored magnetic properties, a potentially important tweaking factor at subcritical particle sizes (less than 20 nm). Monte Carlo simulations demonstrate broader implications for the right kind of defect structure to mediate the magnetic loss mechanisms in favor of efficient energy transfer into heat, even for 10-nm NCs.

II. RESULTS

A. Structural insights

1. Single-particle local structure

Four nanoparticle samples were made available for this study, with specimen of spherical shape, entailing diameters of 8.1 ± 0.6 nm and 15.4 ± 1.3 nm, and of cubic shape, obtaining edge lengths of 12.3 ± 0.7 nm and 17.7 ± 1.6 nm (Fig. S1 in Supplemental Material [44]).

Henceforth, these are called S8, S15, C12, and C18, where S stands for spherical and C for cubic morphologies. Moreover, high-resolution transmission electron microscopy (HRTEM) [Figs. 2(a)—2(d)] suggests that the smaller S8 and C12 NPs entail a domain of a single-phase material, but the bimodal contrast in the larger S15 and C18 points that above a particle size of about 12 nm, two nanodomains are attained. The coexistence of dark and light contrast features in the S15 and C18 could be justified by assuming that two chemical phases, of varying electron diffracting power, share the same nanoparticle volume. Crystallographic image processing by fast Fourier transform (FFT) analysis of the relevant HRTEM images results in their corresponding (spot) electron diffraction patterns [Figs. 2(e)—2(h)]. The unequivocal indexing of reflections in the S8 and C12 specimen may suggest that these adopt the magnetite type of phase [Figs. 2(e) and 2(f)]. On the other hand, a similar conclusion cannot be made after the evaluation of the FFT patterns of the apparently bimodal contrast S15 and C18 specimen, as the cubic spinel and rock salt reflections [Figs. 2(g) and 2(h)] appear to be resolution limited. The behavior appears in line with the tendency of bulk wüstite for oxidative conversion [28,42] and infers a process analogous to its elimination from about 23-nm core@shell $Fe_xO@Fe_{3-\delta}O_4$ nanoparticles [25].

The long- and short-range modulations of the selected (hkl) atomic planes could become more easily isolated with direct space images derived from the inverse FFT synthesis of chosen families of reflections. We find that the (400) [or (200) for the core@shell S15 and C18 NPs] family generates perfect atomic planes (Figs. S2.1–S2.4 in Supplemental Material [44]), and their spacing could be attributed to the $Fe_{3-\delta}O_4$ spinel (or $Fe_{1-x}O$ rock-salt) type of structure. However, the (220) family [Figs. 2(i)—2(l)] deviates from being faultless (Fig. S3). Geometric phase analysis (GPA) [43] of the (220) reflections depicts single-colored regions [Figs. 2(m)—2(p)] that are internally homogeneous, showing no obvious inner-side distortions. The results illustrate a homogeneous structure for the S8 particle (Fig. 2m) but an increasing degree of lattice heterogeneity with size [Figs. 2(n)—2(p)]. GPA has previously pointed to a 5% crystal lattice deformation from (220) planes of about 23-nm $Fe_xO@Fe_{3-\delta}O_4$ nanocubes, while that for the (400) [or (200) for a rock-salt] family amounted to only about 1% [25].

In summary, the evaluation of the number (Nr) of defects involving the (220) planes implies that NPs of spherical morphology (S8, S15) carry a larger number of defects in their volume than the cubic ones, and those of smaller size (S8) are somewhat more susceptible to lattice faults than those of larger size (Fig. S4; Sec. S3 and Table S1 in Supplemental Material [44]). Effectively, such distorted (220) atomic planes [Fig. 1(d)] impose tensile lattice strain as the overall prevailing effect that is pronounced for the spherical morphology (from 4%–5% in the latter, which
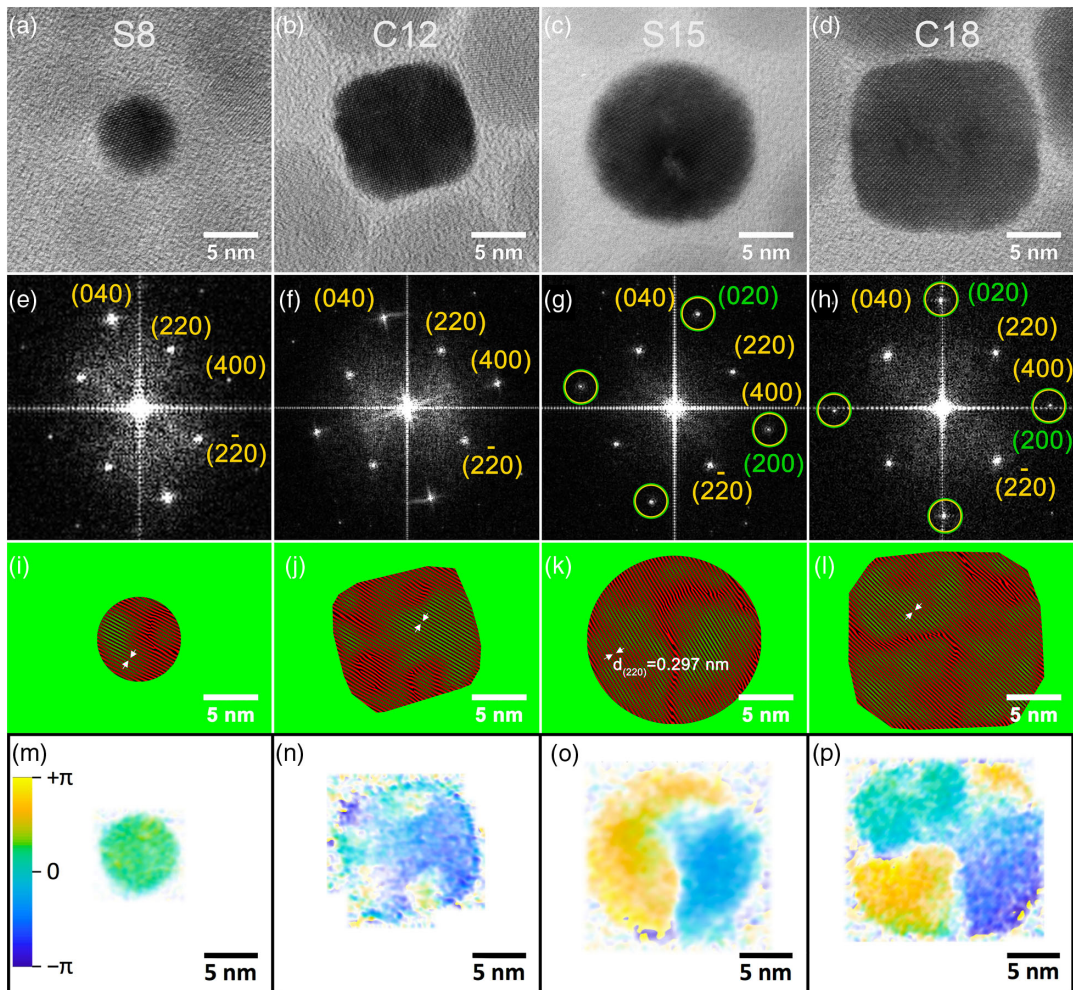
FIG. 2.   High-resolution TEM images in the [001] zone axes for spherical S8 (a), S15 (c) and cubic C12 (b), C18 (d) morphology nanocrystals. The corresponding diffraction patterns (e, f and h, g) after FFT analysis of each micrograph are shown beneath. Green and yellow circles mark a set of reflections that could be indexed on the basis of either wüstite (green) or/and magnetite (yellow) rock-salt and cubic spinel crystal unit cells (see text for details). Representative real-space images of the (220) atomic lattice planes (inverse FFT synthesis; filtered from specific plane orientations) for the samples S8 (i), C12 (j), S15 (k), and C18 (l), respectively. Lattice planes have been colored with red (possible presence of atomic plane) and green (possible absence of atomic plane) pseudochrome acquired after the inverse FFT process. Lattice phase contrast images obtained by the GPA method (see text) after recentering the diffraction around one of the (220) reflections for samples S8 (m), C12 (n), S15 (o), and C18 (p).

drops down to 1%–2% in cubic shape NPs; Sec. S4 and Table S2 in Supplemental Material [44]).

2. Ensemble-average local structure

With the aim of going beyond the HRTEM findings and acquiring quantitative phase-specific structural information from a large ensemble, we measured the synchrotron x-ray PDF of selected nanoparticle specimens and compared them to the bulk magnetite (Fig. 3). As moderate Q space resolution of the experimental setup used limits the PDF field of view in the r space ($r > 5$–10 nm length scales met in bulk), our analysis focuses primarily on the low-r region in the atomic PDF ($r = 1$–10 Å). This method practically allows us to describe the local structure through

insights on bonding and lattice distortions within the $Fe_{3-\delta}O_4$ and Fe_xO unit cells.

Local structure distortions.—Bulk magnetite was taken as a reference system against which subtle distortions of the atomic lattice planes in the nanoparticles could be identified. Initial refinements were performed with the simplified, normal spinel, cubic configuration of magnetite, $(Fe^{3+})_8[Fe^{3+}, Fe^{2+}]_{16}O_{32}$ [45], where the round brackets represent tetrahedral (Td) and the square brackets octahedral (Oh) coordination by oxygen crystallographic sites (i.e., model #1; this case assumes no Fe^{2+}/Fe^{3+} inversion between Td/Oh sites–Table S3, Sec. S5 [44]). The atomic PDF in the low-r region for the bulk sample at 300 K is described well by this
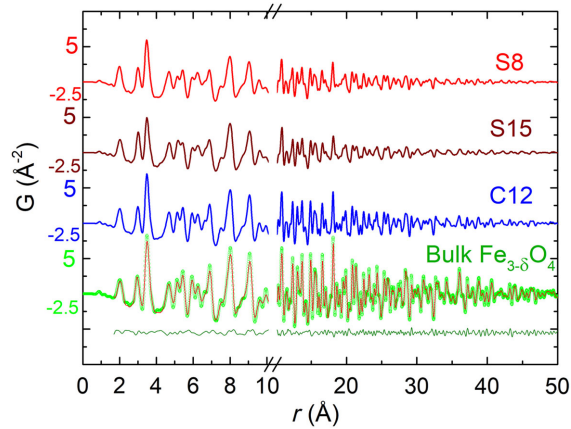
FIG. 3.   Experimental atomic xPDF data at 80 K for the single-phase S8, C12 and core@shell S15 nanoparticles plotted as a function of the radial distance r up to 50 Å. The corresponding xPDF pattern for the bulk magnetite, measured under the same exact conditions, is provided as a reference material. The line over the data is the best fit based on the cubic spinel atomic configuration model (Fd-3m symmetry, model #1, and $R_w =$ 11.6%, the quality of fit factor) and below the corresponding difference between observed and calculated xPDFs for bulk magnetite.

textbook model ($R_w = 8.2\%$). A somewhat lower quality of the fit at 80 K [Fig. 4(a); $R_w = 8.9\%$] may infer some sensitivity to acentric distortions, beyond the r space resolution of our measurements, caused by the Verwey transition of bulk magnetite [46].

The same textbook model (#1) was then utilized to model the xPDF data for nanoparticles of variable size and morphology. What is particularly striking is that between 300 K and 80 K, this cubic model systematically fails to fit the peak at $r \sim 3$ Å [sample S8: Fig. 4(b), $R_w = 18.1\%$; sample C12: Fig. S6(a), $R_w = 11.9\%$]. Importantly, this result corresponds to the closest distance between the iron atoms that are octahedrally coordinated by oxygen in the structure of magnetite [forming a pyrochlore-type sublattice, Fig. 1(d)]. Moreover, the nearest distance of a pair of Fe-Fe in wüstite is also just above 3 Å. It may be expected then that if a detectably large volume fraction of wüstite phase is present in the NPs (cf. HRTEM for S15), then the intensity of the peak at $r \sim 3$ Å should be increased. In an effort to explore this case, a two-phase cubic rock-salt and spinel (FeO-Fe₃O₄) model was employed. This analysis showed that either in smaller nanocrystals (S8 and C12) or larger NPs (S15), the cubic symmetry model [Fig. 4(c); $R_w = 13.6\%$] is somewhat misplaced with respect to the 3 Å observed radial distance distribution. Per the present analysis and assessments of fits over broader r-ranges, it appears that these nanoscale samples are highly nonuniform in terms of defects (see below), and their structure is not quite cubic at high r or locally.

For these reasons, the possibility of the nanoparticle local structure deviating from the ideal cubic lattice

configuration has been factored in. However, the modest Q space resolution for resolving symmetry-lowering configurations beyond the local scale, and, in turn, the limited PDF field of view, led us to utilize approximations implemented by space groups of higher symmetry. The exemplary case of maghemite ($\gamma - Fe_2O_3$) drove this effort, as it can be considered Fe^{2+}-deficient magnetite, $(Fe)_8[Fe_{1\frac{1}{3}}\langle\rangle_{2\frac{2}{3}}, Fe_{12}]O_{32}$ (Fe$_{Oh}$-vacancies represented by the angular $\langle\rangle$ brackets) [47,48]. Under this defect-based scheme, randomly distributed vacancies result in a fcc lattice (model #1), but when their ordering is favored, either a primitive cubic (P4₃32 symmetry, model #2) [49,50] structural variant could be stabilized or a symmetry-lowering lattice distortion is triggered (P4₃2₁2 tetragonal symmetry, model #3) [51,52].

Amongst these models, only model #3 (Table S3, Sec. S5 in Ref. [44]) made a marked improvement in the description of the PDF peak positions from room temperature down to 80 K [Fig. 4d, and Figs. S6(b) and S7(c) in Ref. [44]]. The smaller NPs (≤ 12 nm) were assessed by the PDF (Fig. S5, Sec. S5 in Ref. [44]) to be 100% tetragonal at the local level, while the larger one (S15) entailed a 22.5%:77.5% [rock salt]:[tetragonal] share of volume fractions. The PDF intensities were accurately described when the Fe-site occupancies (η) were refined. The outcome indicates that nanoparticle samples of spherical morphology display the least occupied Fe sites, namely, $\eta - S8 < \eta$-S15 $< \eta$-C12 [i.e., 16.4(1) $<$ 18.2(1) $<$ 20.0(1), out of 24 Fe atoms/unit cell; Fig. S8, Sec. S8 in Ref. [44]]. Along this trend, we find the expansion of the in-plane (a–b) lattice dimensions and the contraction of the c axis, which suggest a more-pronounced tetragonal compression for the spherical (S8, S15 $c/a \sim 0.975$) rather than the cubic (C12, $c/a \sim 0.986$) morphology NPs. Details on the atomic PDF analysis, assessment of the outcomes, and a summary of the derived parameters (Table S4) are presented in the Supplemental Material (Sec. S5) [44].

Though the local symmetry change may be seen as a manifestation of the coupling between elastic and exchange energy terms [53], which are likely optimized by the apparently larger strain in the nanospheres, subtle crystalline electric field effects due to a local tetragonal Jahn-Teller distortion, lifting the orbital degeneracy in Fe^{2+} ($3d^6$) [54], cannot be resolved or ruled out by the structural xPDF probe on this occasion. Moreover, while we cannot completely discard the contribution of valence-swap-induced distortion [with a fraction of Fe^{2+} atoms occupying Fe^{3+} sites and vice versa, cf. $(Fe^{3+})_8[Fe^{3+}, Fe^{2+}]_{16}O_{32}$] [55], we emphasize that vacancy-driven effects are a plausibility as the relative $G(r)$ peak intensities of $Fe_{Oh} - Fe_{Oh}$ ($r \sim 3.0$ Å) and $Fe_{Oh} - Fe_{Td}$ ($r \sim 3.5$ Å) change appreciably (see below), whereas the one-electron difference between the Fe^{2+} and Fe^{3+} electronic configurations would effectively be unobservable in the xPDF peak heights. It is therefore inconceivable that
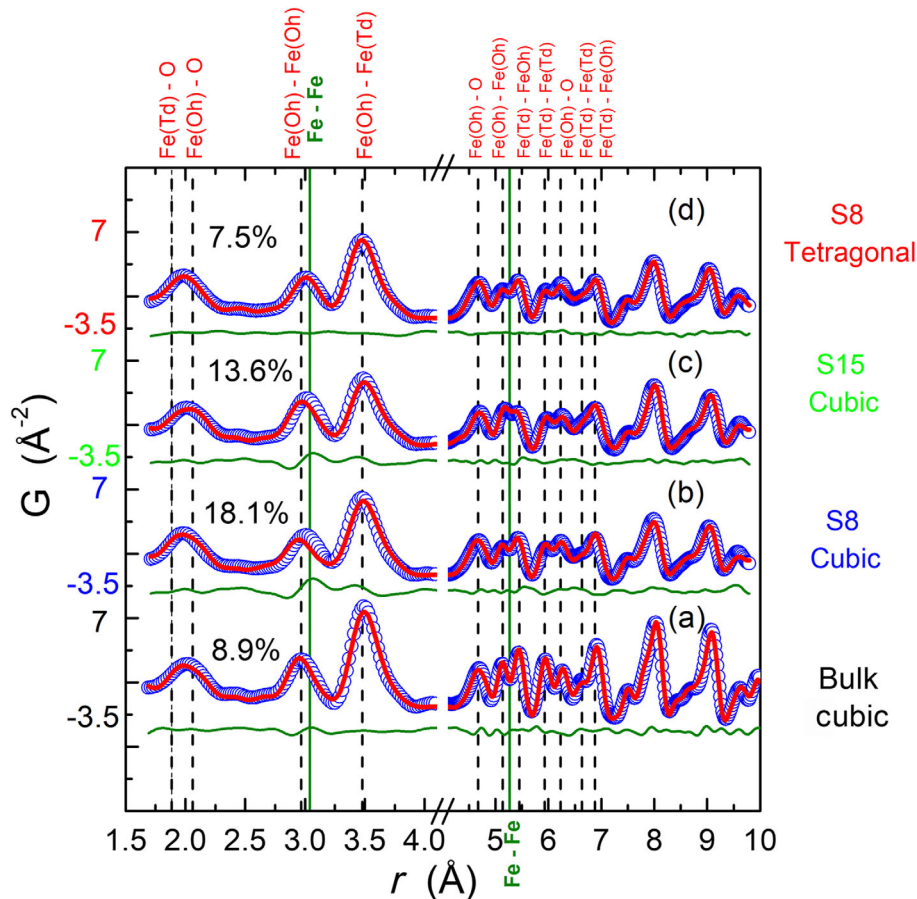
FIG. 4.   Representative xPDF fits ($T = 80$ K) of the "low-r" region for (a) the bulk magnetite assuming the cubic spinel atomic configuration [Fd-3m, model #1; $a = 8.3913(2)$ Å, $R_w = 8.9\%$], (b) the single-phase S8 nanoparticle sample with the same cubic model ($R_w = 18.1\%$), (c) the two-phase S15 nanoparticle sample with the cubic rock-salt and spinel ($R_w = 13.6\%$) crystallographic models, and (d) the single-phase S8 nanoparticle sample in the tetragonal [P4$_3$2$_1$2, model #3; $a_{\mathrm{Sp}} = b_{\mathrm{Sp}} = 8.4053(1)$ Å, $c_{\mathrm{Sp}} = 8.1950(1)$ Å, $R_w = 7.5\%$] crystallographic configuration (see text for details). The blue circles and red solid lines correspond to the observed and calculated atomic PDFs, respectively. The green solid lines underneath are the difference curves between observed and calculated PDFs. The quality of fit factor, R_w (%), is given for each case. Vertical dashed lines mark the positions of typical Fe─O and Fe─Fe bond distances; Td and Oh represent tetrahedral and octahedral cation sites, respectively.

observed dramatic changes in relative PDF peak intensities originate from inverted-spinel-like electronic configurations.

Recapitulating the above PDF analysis, it is important to recognize the sensitive nature of the NPs, and especially those with spherical shape, in the local structure non-stoichiometry. Fe vacancies stabilize a tetragonally distorted local structure, inferring a relation to the large number of defects in the crystal volume, as implicated by the HRTEM-based analysis as well. Our results, albeit based on just two single-phase specimens, suggest enhanced tetragonalicity for spherical nanoparticle morphology.

Where the defects are located.—The question as to how structural vacancies relate to different cation lattice sites is now tackled by comparing the observed, normalized $G(r)$ patterns of the NPs against the bulk magnetite [Fig. 5(a)]. Two types of radial distance populations, represented by

the $G(r)$ peak intensity, are considered. (a) Fe$_{\mathrm{Oh}}$ − Fe$_{\mathrm{Oh}}$ separations ($r \sim 3.0$ Å): When the single-phase NPs peak-intensity maximum is compared to that in the bulk stoichiometric Fe$_3$O$_4$, a measure of the presence of Oh vacancies is witnessed. With ratios of about 0.8 and 0.9, for the S8 and C12 NPs, respectively, more Oh-Fe vacancies are supported in the nanospheres. For the larger NPs (S15), the enhanced $G(r)$ suggests an increased rock-salt type of phase in their volume. (b) Fe$_{\mathrm{Oh}}$ − Fe$_{\mathrm{Td}}$ separations ($r \sim 3.5$ Å): The progressive diminution of the $G(r)$ peak intensity also advocates that the spherical nanoscale morphology (S8, S15) adopts noticeably more empty lattice sites than the cubic one (C12), conferring that their abundance is a shape-dependent phenomenon [10].

With the purpose of further evaluating if the vacancies have a site-specific preference, xPDF patterns were simulated, while the ratio of Fe-vacancy population at the Oh
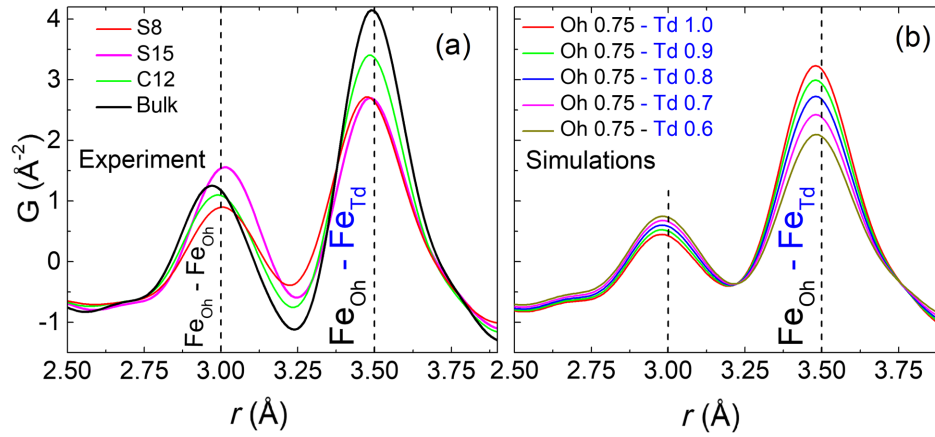
FIG. 5. (a) Adequately normalized, observed $G(r)$ patterns ($T = 80$ K) of the low-r region for all nanoparticle samples (single-phase, S8 and C12, and two-phase, S15) compared against the bulk magnetite and (b) the simulated xPDF patterns on the basis of the symmetry-lowering (tetragonal) atomic configuration. As a proof of concept, the optimally chosen set of models assumes a substoichiometric Oh Fe-site occupancy (η; kept constant at 75%, an average occupation derived from refinements of the $G(r)$ data across the samples), while the Td Fe-site occupation level is varied in a stepwise manner ($60 < \eta < 100\%$). Vertical dashed lines mark the modification of the distribution of the $\text{Fe}_{\text{Oh}} - \text{Fe}_{\text{Oh}}$ ($r \sim 3.0$ Å) and $\text{Fe}_{\text{Oh}} - \text{Fe}_{\text{Td}}$ ($r \sim 3.5$ Å) separations from bulk to nanoscale samples.

and Td sites was varied. The trend is similar assuming either the symmetry-lowering model #3 [Fig. 5(b)] or the cubic spinel model #1 [Figs. S9(b) and S9(c); Sec. S9 [44]). The progressive intensity diminution at $r \sim 3.5$ Å, when raw and simulated patterns are compared, corroborates with a significant volume of vacancies also at the Td Fe sites (about 10%–20%; Fig. S8 [44]), inferring a limited length of structural coherence [56]. This result is in contrast to bulk spinel samples where intrinsic Oh Fe vacancies mediate the structure and properties [57]. The significant content of vacancy distribution resolved by xPDF may infer emerging strains or stresses (Fig. S10 and Sec. S10 [44]), reminiscent of those in $\text{Fe}_x\text{O@Fe}_3\text{O}_4$ nanocubes probed by single-particle local structure techniques [25,29].

Overall, the PDF indicates that during the self-passivation of wüstite, smaller NPs are single phase while larger ones attain a two-phase character. This size-mediated phase evolution is in agreement with the HRTEM findings, which also indicate that particles of spherical shape accommodate a larger number of defects in their volume [cf. xPDF refined Fe-site occupancy $\eta-$S8 $< \eta$-S15 $< \eta$-C12, i.e., $16.4(1) < 18.2(1) < 20.0(1)$, where $\eta = 24$ Fe atoms/unitcell of the bulk cubic spinel; Fig. S8 [44]]. In addition, the PDF uncovers the fact that in addition to vacancies commonly found at the Oh sites, Td-Fe is largely absent, fostering local tetragonal lattice distortions. These observations trigger questions about the impact of vacancies on the observed properties.

B. Nanometer scale effects on properties

1. Magnetic behavior

In view of the nanoparticles' deviation from perfect structural ordering, their magnetic behavior is evaluated

here because of its direct relevance to hyperthermia applications. A broad maximum in the dc magnetic susceptibility, $\chi(T)$, with an irreversibility between ZFC/FC curves [Figs. 6(a)—6(c); Fig. S11(a) [44]], marks a characteristic temperature T_B that separates the superparamagnetic state from the blocked state [5]. In addition, the $\chi(T)$ for the core@shell NPs [S15 [44]; Fig. 6(c)] points to a sudden drop due to the paramagnetic-to-AFM transition (T_N) in wüstite and a subtle anomaly resembling the Verwey transition (T_V) of bulk magnetite [30,35,36]. Furthermore, the evolutions of the hysteresis loop characteristics (Sec. S11, Table S5; Figs. S11(b) and S11(c) in Supplemental Material [44]) suggest that a process beyond the coherent reversal of M is involved. In this process, $M(H)$ experiments under field cooling [$H_{\text{cool}} = 50$ kOe; Figs. 6(d)—6(f), Figs. S12 and S13 [44]] support the development of a macroscopic, exchange-bias field (H_{EB}) resulting from interfacial interactions [16]. The quick rise of H_{EB} for the S15 NPs, against the single-phase S8 and C12 (Fig. 7, and Fig. S14, Sec. S14 [44]), implies competing exchange interactions due to different kinds of interfaces.

In addition, all the NPs present a discontinuous steplike variation of the magnetization near zero field [Figs. 6(d)—6(f), Fig. S13 [44]]. The two switching field distributions, marked by maxima in dM/dH, resemble the inhomogeneous magnetic behavior arising from coexisting magnetic components of contrasting H_Cs (e.g., of mixture of particle sizes [58] or compositions [59]). Here, though, the HRTEM study of the $\text{Fe}_x\text{O} - \text{Fe}_3\text{O}_4$ NPs confers their single-crystal character and narrow particle-size distribution (Fig. S1 [44]). However, xPDF resolves Fe-site vacancies [$V = (\eta - $S8 or η-S15 or η-C12)$:\eta$ is the
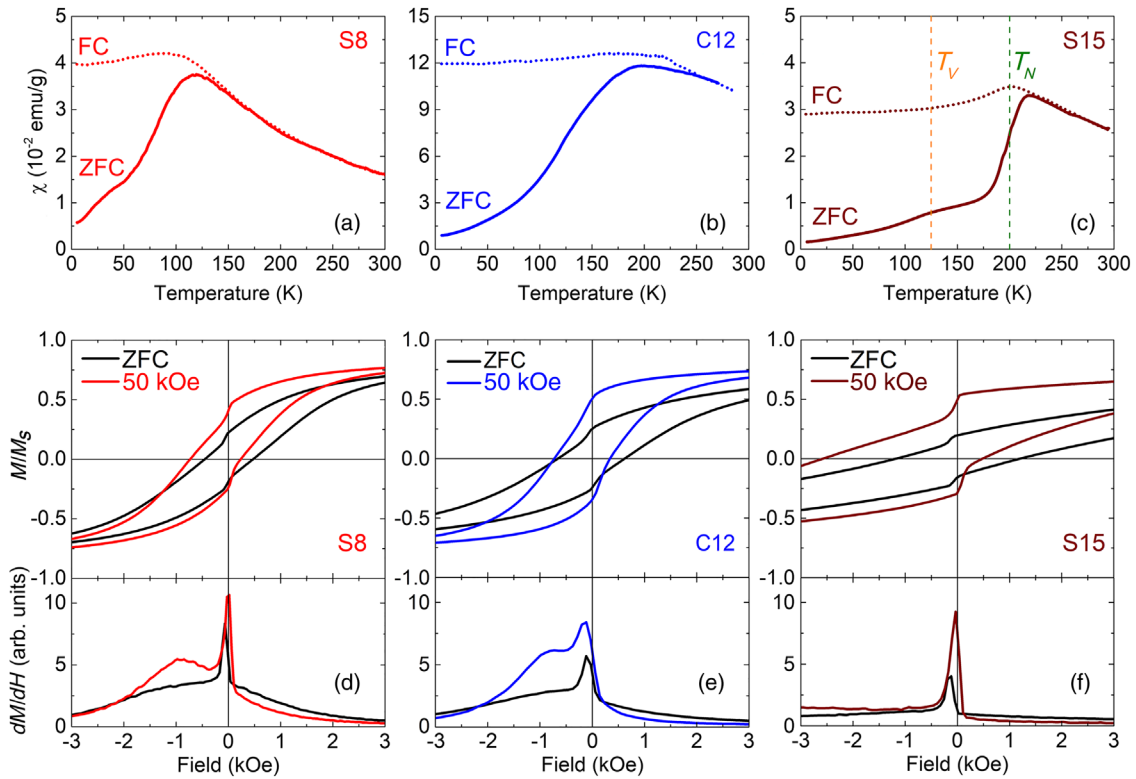
FIG. 6. The temperature evolution of the zero-field cooled (ZFC; solid lines) and field-cooled (FC; dotted lines) susceptibility curves for the single-phase S8 (a), C12 (b), and core@shell S15 (c) nanoparticles under a magnetic field of 50 Oe. The dashed vertical lines indicate the Verwey (T_V; orange) and Néel (T_N; green) related transition temperatures met in bulk, stoichiometric Fe_3O_4 and Fe_xO, respectively. The low-field part of the normalized hysteresis loops (M/M_S) at 5 K for the single-phase S8 (d), C12 (e), and the core@shell S15 (f) nanoparticles taken under zero- and field- cooled ($H_{cool} = 50\,kOe$) protocols. The panels beneath the loops present the differential change (dM/dH) of the normalized, isothermal magnetization when it is switched from positive to negative saturation.

modeling-derived content per unit cell volume, $\eta =$ 24 Fe atoms/cell of bulk cubic spinel], with $V-S8(33\%)> V-S15(25\%)>V-C12(17\%)$. The existence of these defects seems to establish a spatial variation of the composition at the local level that "turns on" the observed inhomogeneous magnetism.

2. Coupling of structural defects to magnetism

To shed light on how atomic-scale defects (e.g., Td Fe-lattice site vacancies and local tetragonal distortions) couple to magnetism, we utilize Monte Carlo (MC) simulations. For this purpose, our systems are approximated by a microscopic "core-surface" model [60,61], however, with random defects introduced in the nanoparticle structure. These defects were described as weakly coupled FM pairs of spins with strong anisotropy, inferred from the symmetry-lowering local structure (Sec. II A 2) of the NPs. Their soft FiM character [62] was chosen to resemble that of $V_4 - Td$ clusters of defect units [due to coalescence of four Fe_{Oh} vacancies (V) around an Fe^{3+}_{Td} interstitial] [Figs. 1(b) and 1(c)] [28] out of which spinel magnetite has been claimed to nucleate during the oxidative conversion of Fe_xO [63]. Assuming that the

fraction of the FM pairs of spins (pinning bonds) is a tunable particle parameter, associated with the xPDF-derived Fe vacancies, the evolution of (a) the low-field jump ($\Delta M/M_S$, estimates how many magnetic moments are switched) and (b) the exchange bias (H_{EB}) have been quantified (Fig. 8).

With the purpose of assessing the former, $\Delta M/M_S$, we note that the surface is large for the smaller nanoparticles, i.e., about 50% of the S8 and about 35% of the C12 specimens, and both may assume a two-phase magnetic nature. The $\Delta M/M_S$ changes may then be a manifestation of the character stemming from the exchange-coupled hard and soft ferromagnetic and ferrimagnetic phases in the two nanodomains [64]. As the number of pinning bonds (vacancy driven) increases in the main body of these NPs, MC calculations point to the fact that the defects' strong random anisotropy leads to exchange randomness, rendering their two-phase magnetic nature more disordered. This result leads to less prominent $\Delta M/M_S$ changes in the hysteresis loops (Fig. 8). Considering the evaluation of the latter, we note that the defect-induced spin disorder within the corelike subdomains reduces the overall magnetization (Fig. S12 [44]) but supports extra pinning centers
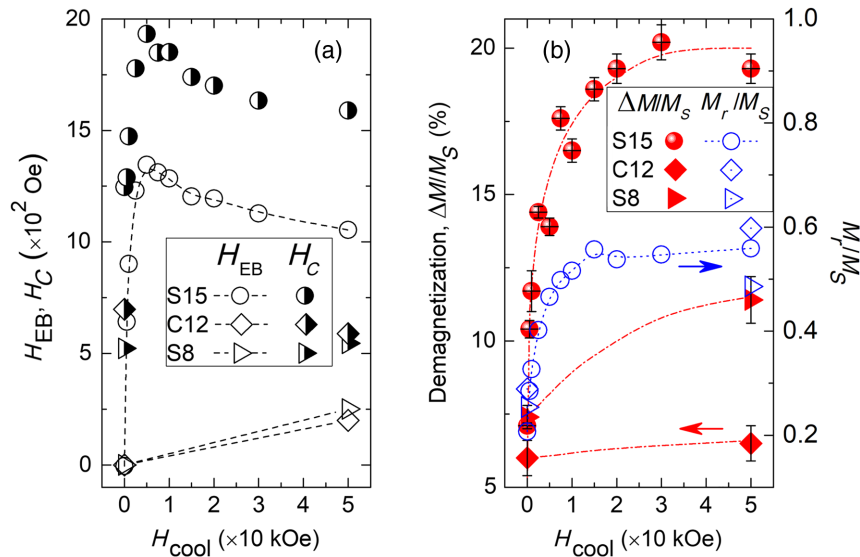
FIG. 7. The experimentally determined (a) exchange bias (H_{EB}; open symbols) and coercive field (H_C; half-filled symbols), as well as (b) low-field demagnetization ($\Delta M/M_S$; filled symbols, left y axis) and the ratio M_r/M_S (M_r, remanence: open symbols, right y axis) obtained at varying cooling-field strengths (H_{cool}). Symbol guide: circular, core-shell spherical nanoparticles (S15), triangular (S8), and diamond (C12) for single-phase spherical and cubic morphology nanoparticles. The lines are a guide to the eye.

that could foster a density of uncompensated interfacial spins, impeding easy coherent reversal [65] of the surrounding ferrimagnetic moments (Fig. S13 [44]). In line with this case are the MC simulations, which indicate that in small S8 and C12 NPs without defects, exchange bias is absent, but when the perturbation of the periodic potential of the iron coordination by lattice defects is enabled, the
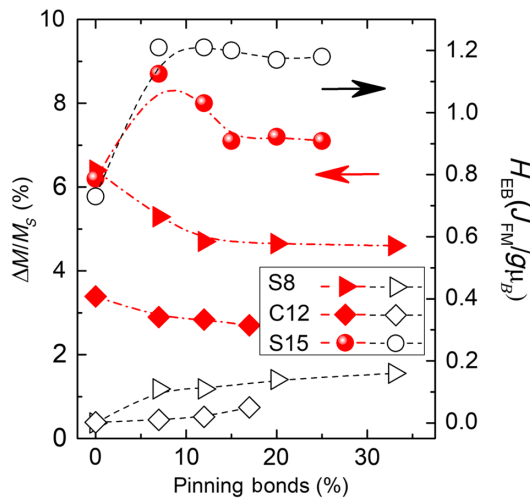

FIG. 8. Monte Carlo calculations ($H_{cool} = 5\, J_{FM}/g\mu_B$) of the effect of pinning bonds (vacancy-driven) on the low-field magnetic-moment switching ($\Delta M/M_S$; filled symbols, left y axis) and the exchange bias (H_{EB}; open symbols, right y axis) of self-passivated $Fe_x O - Fe_3 O_4$ nanocrystals with different morphologies. Symbol guide: circular, core-shell spherical nanoparticles (S15), triangular (S8), and diamond (C12) for single-phase spherical and cubic-shape nanoparticles.

increasing number of pinning bonds in the core results in net exchange bias (Fig. 8).

The behavior is depicted in the magnetic-moment snapshots of defected [Figs. 9(a)—9(c)] versus defect-free [Figs. 9(d)—9(f)] NPs. While for nondefected NPs the soft anisotropic core follows the applied field reversal, the existence of defects generates localized antiparallel spin components, which couple to neighboring ferrimagnetic spins at the atomic-scale interface and promote the canting of the core towards the xy plane (snapshots of the spin ensemble under a full M-H loop are compiled in Fig. S15, while the mean moment orientation is shown in Fig. S16 [44]). In this way, the nanospheres' more defected internal structure generates adequate conditions that endorse exchange coupling so that $H_{EB} - S8 > H_{EB} - C12$ (while $H_C - S8 < H_C - C12$, due to differences in the NPs' magnetic volumes). As magnetization states at the different kinds of interfaces are adjusted by H_{cool}, for a matter of consistency, it is worth pointing out that MC simulations (Fig. S17 [44]) reproduce fairly well the experimental (Fig. 7) evolution of the hysteresis loop parameters (H_{EB}, H_C, $\Delta M/M_S$) even for the larger S15 NPs (Sec. S17 [44]).

The defect-rich NPs discussed here broaden the picture that growth-approach-mediated, subtle, structural microscopic factors [24,33,66] foster local-scale anisotropy that facilitates exchange bias in otherwise phase-pure, monocrystalline NCs.

3. Defect-driven magnetic heating

The observed evolutions may be related to structural and morphological variations between NPs exhibiting differences in size, surface anisotropy, and exchange
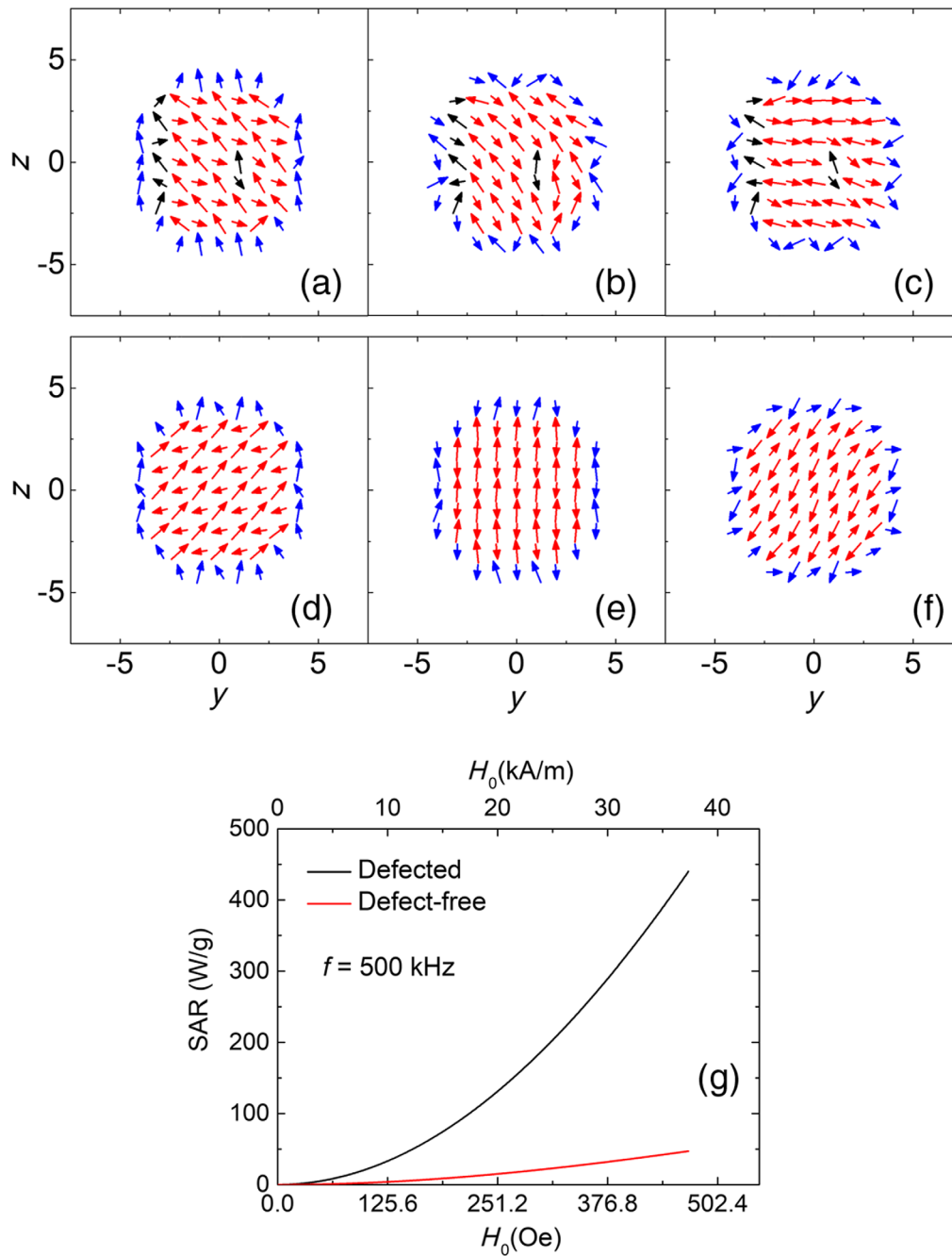
FIG. 9. MC simulation of the $M - H$ loops made after field-cooling ($H_{cool} = 5\ J_{FM}/g\mu_B$) and by assuming an upper maximum fraction of pinning bonds, as this was identified by the xPDF refinements. Snapshots of the spin ensemble during $M - H$ loop calculation for a small ferrimagnetic spherical nanoparticle of $R = 5$ lattice constants: (a)—(c) a fully oxidized, defected nanocrystal (S8), and (d)—(f) a defect-free case, assuming a core-surface type of MC model. Spin configurations are shown in the zy plane ($x = -1$) for positive-field ($H = +8\ J_{FM}/g\mu_B$) magnetization saturation and after field reversal ($H = -0.2\ J_{FM}/g\mu_B$, $H = -2.0\ J_{FM}/g\mu_B$) towards negative saturation. The arrow color coding is as follows: core (red), surface (blue), and defects (black) magnetic moments. (g) Specific absorption rate (SAR) of small defected (S8) versus defect-free nanoparticles on the basis of susceptibility losses (ac field amplitude, H_0 and $f = 500$ kHz), calculated according to the linear response theory of a modified Néel-Brown relaxation Monte Carlo model.

anisotropy. Ferrite nanocrystals, in magnetically mediated biomedical applications, draw their versatility from the critical particle size (about 20 nm) [39], a factor that varies with the magnetic anisotropy [41]. In the present work, we have demonstrated that surface atoms can respond differently than the core ones, a prominent effect for the smaller fully oxidized derivatives (≤ 12 nm) of the $Fe_xO - Fe_{3-\delta}O_4$ NCs. Although defect elimination during synthesis can yield nanomagnetic agents (≥ 20 nm) with enhanced, concurrent diagnostic imaging and thermo-responsive performances [34], structural defects at subcritical particle sizes appear to offer a different exploitable pathway, compatible with the biological limits (e.g., set by toxicity and patient discomfort) [67]. Here, vacancies in self-passivated iron oxides of subcritical size (≤ 12 nm) act as pinning centers that favor the competition of exchange interactions, thus fostering local anisotropy enhancement. Benefits from the NPs' extended anisotropic properties may raise their application potential–for example, to afford heat generation beyond the bare susceptibility losses (Néel-Brown relaxation) mediated by finite-size effects alone (Sec. S18 [44]). [40].

The MC simulations support the fact that for small defected NPs (S8), where the effective anisotropy increases 5 times compared to the defect-free ones, the heat dissipation (specific absorption rate=SAR) is raised almost tenfold, i.e., about 450 W/g vs about 50 W/g, at 500 kHz under 37.3 kA/m [Fig. 9(g)]. For comparison, it is worth noting that, experimentally, defect-free 9-nm Fe_3O_4 NPs exhibit a SAR of 152 W/g [14]. It can be envisaged then that nanoparticle self-passivation leads to adequate perturbation of the periodic potential of the iron coordination by vacant lattice sites that, in turn, tweak the core-to-surface magnetic anisotropy ratio. Whether this might be an avenue to boost the thermal energy transfer at subcritical particle sizes (≤ 10 nm) by synergistic relaxation processes warrants further exploration. Even in the absence of extended buried AFM/FM interfaces [14], where beneficial exchange parameters attain efficient heat sources, smaller heterogeneous nanocrystals (S8, C12) may be uncovered as useful heat-therapeutic agents.

III. CONCLUSIONS

The self-passivation of nanoscale wüstite (Fe_xO) has been investigated as a testing ground to explore the consequences of thermodynamically unstable interfaces formed during the nucleation and growth of nanostructured iron oxides. As conventional oxidation evolves, grown component phases give rise to single-crystal nanoscale entities with subdomain $Fe_xO - Fe_{3-\delta}O_4$ interfacial connectivity. However, when the synthesis parameters are varied to attain smaller-size nanocrystals (≤ 12 nm), a spinel-like phase is nucleated alone. The compositional and structural complexity of these iron-oxide nanostructures is witnessed by single-particle transmission electron

microscopy and complementary, phase-specific structural information, attained from a large ensemble by high-energy synchrotron, x-ray total scattering experiments. These experiments uncover the fact that defects (with a significant volume residing at tetrahedral Fe sites) alleviate a surprising tetragonal lattice compression in the spinel-like phases. The defects entail structural vacancies with an increased number density when the nanoscale morphology changes from cubic to spherical and the particle size shrinks. Moreover, magnetometry and Monte Carlo calculations show that the nanostructures' heterogeneous character is demonstrated by a core-surface type of spin configuration that favors two switching field distributions. Larger core@shell $Fe_xO - Fe_{3-\delta}O_4$ nanocrystals support exchange bias due to the coupling across a common interface of spatially extended subdomains of AFM and FiM nature. Exchange bias is unexpectedly evident, though much reduced, in smaller-size (≤ 12 nm), fully oxidized particles, due to the existence of the defected internal structure that generates localized antiparallel spin components and uncompensated spin density at atomic-scale interfaces. The latter, in line with the noncubic local symmetry of the nucleated spinel phases, expresses the influence of local anisotropy fields, which apparently deviate from the easy-axis symmetry met in common iron oxides, favoring canting into the xy plane. The results corroborate that size-dependent evolution of the metal-cation valence state produces pinning defects that promote the competition of the exchange interactions at subcritical sizes (<20 nm). The concept raised here points to the fact that atomic-scale defect control in small particles (~ 10 nm), typically hampered by the superparamagnetic limit, may act in favor of anisotropic properties for improved magnetism-engineered functionalities (cf. heating agents and thermoresponsive cellular processes).

IV. METHODS

A. Materials

All reagents were used as received without further purification. Oleic acid (technical grade, 90%), absolute ethanol ($\geq 98\%$), octadecene (technical grade, 90%), hexane (ACS reagent, $\geq 99\%$), and sodium oleate powder (82%) were purchased from Sigma Aldrich. Iron (III) chloride ($FeCl_3 \cdot 6H_2O$, ACS Reagent) was purchased from Merck. Iron (III) acetylacetonate was purchased from Alfa Aesar, and oleylamine 80%–90% was purchased from Acros Organics.

B. Syntheses protocols

Colloidal syntheses were carried out in 100-mL round-bottom three-neck flasks connected via a reflux condenser to a standard Schlenk line setup, equipped with immersion temperature probes and digitally controlled heating mantles. The reactants were stored under anaerobic conditions

in an Ar-filled glovebox (MBRAUN, UNILab), containing less than 1 ppm O_2 and H_2O.

A gas mixture of 5% H_2/Ar has been used as a protective/reductive atmosphere. The reductive atmosphere can help us to maintain the Fe_xO (wüstite) phase instead of the oxidized Fe_3O_4 (magnetite) and/or $\gamma - Fe_2O_3$ (maghemite) forms. Previous studies have shown that Fe_xO crystallites formed under these synthetic conditions become rapidly oxidized after removing the reducing agent and exposing them to ambient air [68]. Very small particles tend to be fully oxidized to the spinel structure. A minimum diameter over about 13 nm is needed for the nanoparticle to maintain its core@shell structure.

1. Preparation of iron oleate precursor

Iron (III)-oleate was prepared before each nanoparticle synthesis and subsequently used as an iron precursor. Special care was taken to protect it from the light. The metal oleate precursor was formed by the decomposition of $FeCl_3 \cdot 6H_2O$ in the presence of sodium oleate at 60 °C, based on a slightly modified literature protocol [69]. Here, 16 mmol of $FeCl_3 \cdot 6H_2O$ salt and 48 mmol of sodium oleate were dissolved in a mixture of solvents in a round bottom flask, and 56 mL hexane, 32 mL ethanol, and 24 mL distilled water were used as solvents. The mixture was heated to 60–65 °C under Ar atmosphere for 4 hours and then left to cool down to room temperature. The organic phase containing the metal oleate complex was separated from the aqueous phase using a separatory funnel and then washed with about 30 mL distilled water and separated again. This process was repeated 4 times, and at the end, the metal-organic complex was dried under stirring and mild heating for several hours, resulting in a viscous dark-red oleate. The final product was stored in a dark place to protect it from light. Some mild heating to ensure its fluidness may be needed just before its use for each nanoparticle synthesis. The successful fabrication of the ferric oleate complex has been identified by the FTIR data (Fig. S19 [44]) [70].

2. Synthesis of iron-oxide nanoparticles

The NPs were synthesized by employing modified literature protocols [18,35,70,71] aiming to produce the wüstite type of oxide ($Fe_{1-x}O$). In a typical synthesis, 2–7 mmol of iron oleate were dissolved in octadecene in a flask under a reductive atmosphere. Oleic acid was used as a surfactant and protective ligand, in a proportion 1:2 with respect to the iron precursor. The amounts of reactants were tuned so that a final Fe-oleate molar ratio of 0.2 mol/kg solution was achieved. The synthesis protocol includes three major steps. First, a degassing step at 100 °C for 60 min under vacuum is required for the complete removal of any water and oxygen residues. Then, the mixture is heated to 220 °C, with a heating rate of about 10 °C · min^{-1}. At this temperature, which lasts for 60 min,

the so-called nucleation step allows for the crystal seeds [92] to be generated for the successive formation of the NCs. At the final stage, the mixture is heated to 320 °C, where the nanocrystals' growth takes place. At the end of the synthesis, the colloidal mixture was left to cool down at room temperature, and the NCs were precipitated upon ethanol addition. They were separated by centrifugation at 6000 rpm for 5 min, redispersed in hexane, and then centrifuged once more after adding ethanol in a 1:1 ratio with respect to the hexane. The process was repeated two more times at a centrifugation speed of 1000 rpm. The addition of sodium oleate proved to promote the formation of cubic NPs, as proposed in earlier studies [71]. We found that a metal-precursor-to-sodium-oleate ratio of 8:1 to 5:1 is adequate enough to realize such a shape transformation. Minor variations in this two-step heating protocol allow the tuning of the particles' size and the control of their size distribution [18,72]. The protocol gives rise to NPs with diameters up to 20 nm, with size control attained by modifying the growth time ($40 < t < 90$ min) at the final stage. An extended stay here produces even larger NPs, but beyond 60 min, smaller-size particles are afforded, likely due to a ripening mechanism. Four iron-oxide colloidal nanostructures, with varying size and morphological features (see above), S8, C12, S15, C18 (S: spherical, C: cubic), were finally grown and stored as colloidal dispersions in about 4 mL hexane in septa-sealed vials.

C. Characterization techniques

1. High resolution transmission electron microscopy

Low-magnification and HRTEM images were recorded, using a LaB_6 JEOL 2100 electron microscope operating at an accelerating voltage of 200 kV. All the images were recorded by the Gatan ORIUS^{TM} SC 1000 CCD camera. For the purposes of the TEM analysis, a drop of a diluted colloidal nanoparticle solution was deposited onto a carbon-coated copper TEM grid, and then the hexane was allowed to evaporate. In order to estimate the average size, statistical analysis was carried out on several low-magnification TEM images, with the help of the dedicated software ImageJ [73]. The structural features of the nanoparticles were studied by two-dimensional (2D) FFT images acquired and analyzed by ImageJ.

With the purpose to highlight the defect structure of the nanoparticles, we employed the geometric phase analysis (GPA) method of Hÿtch *et al.* [43]. The HRTEM images were Fourier transformed, and a region around one of the {220} peaks was selected with a circular window. This diffraction pattern was recentered and inverse Fourier transformed to provide a real-space image whose phase [Figs. 2(m)—2(p)] represents the projection (onto the {220} reflection chosen) of the lattice shift of that particular region of the crystal relative to the average lattice. The single-colored regions are internally

homogeneous, showing no obvious internal distortions, but have different phase shifts from their neighbors.

2. X-ray pair distribution function

X-ray synchrotron-based PDF data were acquired at the 28-ID-2 beamline of the National Synchrotron Light Source II, Brookhaven National Laboratory. Each nanoparticle powder was encapsulated in a $\varnothing 1.0$ mm kapton capillary, sealed at both ends with epoxy glue. The 28-ID-2 in PDF mode used a Perkin-Elmer 2D image plate detector for fast data acquisition but of relatively modest Q space resolution, which, in turn, limits the PDF field of view in r space. Data were collected between $80 < T < 400$ K, making use of the beamline's liquid nitrogen cryostream (Oxford Cryosystems 700), with incident x-ray energy of 68 keV. Bulk magnetite powder (Fe_3O_4) was utilized as a reference.

The atomic PDF [39] gives information about the number of atoms in a spherical shell of unit thickness at a distance r from a reference atom and is defined as

$$G(r) = 4\pi r[\rho(r) - \rho_0] \quad (1)$$

where ρ_o is the average number density, $\rho(r)$ is the atomic pair density, and r represents radial distance. The raw 2D experimental data are then converted to 1D patterns of intensity versus momentum transfer, $Q (= 4\pi \sin\theta/\lambda)$, which are further reduced and corrected using standard protocols, and then finally Fourier transformed to obtain $G(r)$:

$$G(r) = (2/\pi) \int_{Q_{min}}^{Q_{max}} Q[S(Q) - 1] \sin(Qr)dQ. \quad (2)$$

$S(Q)$ is the properly corrected and normalized powder diffraction intensity measured from Q_{min} to Q_{max}. The experimental PDF, $G(r)$, can subsequently be modeled by calculating the following quantity directly from a presumed structural model:

$$G(r) = \left[\frac{1}{r} \sum_{ij} \frac{f_i f_j}{\langle f \rangle^2} \delta(r - r_{ij}) \right] - 4\pi r\rho_0. \quad (3)$$

Here, f stands for the x-ray atomic form factors evaluated at $Q = 0$, r_{ij} is the distance separating the ith and jth atoms, and the sums are over all the atoms in the sample. In the 28-ID-2 experiments, elemental Ni powder was measured as the standard to determine parameters, such as Q_{damp} and Q_{broad}, to account for the instrument resolution effects. Experimental PDFs, based on modest Q space resolution and $Q_{max} = 25$ Å^{-1} raw powder diffraction data, were fitted with structural models using the PDFgui [74] software suite.

3. Magnetic measurements

The magnetic characterization was conducted using a vibrating sample magnetometer (VSM, Oxford Instruments, Maglab 9T), operating at a vibration frequency of 55 Hz. The measurements of the temperature-dependent magnetization, $M(T)$, were carried out at 50 Oe at a fixed temperature rate of 1 K min^{-1} after either zero-field cooling (ZFC) or field cooling (FC) in 50 Oe from 300 K to 5 K. Selected $M(T)$ measurements were also carried out at a different applied field (100 Oe). Hysteresis loops, $M(H)$, were obtained at room temperature and at 5 K by sweeping the applied field from $+50$ kOe to -50 kOe and back to $+50$ kOe after cooling the sample from 300 K to 5 K under ZFC or an applied field $0 < H_{cool} \leq 50$ kOe (FC). In the FC procedure, once the measuring temperature was reached, the field was increased from H_{cool} to $H = 50$ kOe, and the measurement of the loop was pursued. Because of a small remnant field, common in superconducting magnets, the values of the coercive field (Table S5 in Supplemental Material [44]) have been corrected, as [magnetometer reported field] + [field error] = [real magnetic field at the sample]. The offset error in the magnetic field (max 60 Oe) was estimated through the "field error vs charge field" calibration chart of the magnetometer. Although such an amendment does not propagate to the extracted exchange-bias values, it has been taken into account in the low-field demagnetization ($\Delta M/M_S$) and the ratio of remanence against saturation (M_r/M_S) (Fig. 7). In addition, when data are recorded under a magnetic field sweep, a synchronization error of the measuring electronics can be observed if high sweeping rates, larger than 200 Oe/s, are chosen. To avoid this artifact, we evaluated $M(H)$ loops collected at step mode versus sweeping, at various rates, and found that a sweeping rate of 30 Oe/s provides adequate conditions to minimize the error propagation in the measurements.

While precautions were taken to maintain the integrity of the samples, their spontaneous chemical evolution led us to exclude one specimen (C18) from the in-depth discussion where magnetism and structural properties are correlated (Sec. II B). This is because, while TEM structural investigations were pursued soon after the sample growth, neither xPDF nor magnetic characterizations were readily available (due to remote facility timeline access restrictions) near the initial lifetime of the samples. So, while four iron-oxide colloidal nanostructures were grown initially, their self-passivation into $Fe_xO - Fe_3O_4$ nanocrystals led us to discuss magnetic data (Fig. S11 [44]) only for three samples (i.e., S8, C12, S15), which allowed a coherent picture of their structure-property relations to be attained.

D. Monte Carlo simulations

The simulations approximate the NPs by a microscopic "core-surface" model [60,61]. Three nanoparticle model

systems were considered, with somewhat different morphological features, as these were probed experimentally in the S8, C12, and S15 specimens. The spins in the NPs were assumed to interact with nearest-neighbor Heisenberg exchange interaction, and at each crystal site, they experience a uniaxial anisotropy [35,75,76]. Under an external magnetic field, the energy of the system is calculated as

$$E = -J_{\text{core}} \sum_{i,j \in \text{core}} \vec{S}_i \cdot \vec{S}_j - J_{\text{shell}} \sum_{i,j \in \text{shell}} \vec{S}_i \cdot \vec{S}_j - J_{\text{IF}} \sum_{i \in \text{core}, j \in \text{shell}} \vec{S}_i \cdot \vec{S}_j$$
$$- K_{i \in \text{core}} \sum_{i \in \text{core}} (\vec{S}_i \cdot \hat{e}_i)^2 - K_{i \in \text{shell}} \sum_{i \in \text{shell}} (\vec{S}_i \cdot \hat{e}_i)^2 - \vec{H} \sum_i \vec{S}_i. \tag{4}$$

Here, $\vec{S}_i$ is the atomic spin at site i, and $\hat{e}_i$ is the unit vector in the direction of the easy axis at site i. The first, second, and third terms give the exchange interaction between spins in the AFM core, in the FiM shell, and at the interface between the core and the shell, respectively. The interface includes the last layer of the AFM core and the first layer of the FiM shell. The fourth and fifth terms give the anisotropy energy of the AFM core, K_C, and that of the FiM shell, K_{shell}, correspondingly; the last term is the Zeeman energy.

Parameters were chosen (Sec. S20 in Supplemental Material [44]) after careful analysis of the experimental magnetic behavior, and MC simulations were implemented with the Metropolis algorithm [77]. The hysteresis loops $M(H)$ were calculated upon a field-cooling procedure, starting at a temperature $T = 3.0 \, J_{\text{FM}}/k_B$ and down to $T_f = 0.01 \, J_{\text{FM}}/k_B$, at a constant rate under a static magnetic field H_{cool}, directed along the z axis. The hysteresis loop shift on the field axis gave us an estimate of the exchange field, $H_{\text{EB}} = -(H_{\text{right}} + H_{\text{left}})/2$. The coercive field was defined as $H_C = (H_{\text{right}} - H_{\text{left}})/2$. Note that H_{right} and H_{left} are the points where the loop intersects the field axis. The fields H, H_C, and H_{EB} are given in dimensionless units of $J_{\text{FM}}/g\mu_B$, the temperature T in units J_{FM}/k_B, and the anisotropy coupling constants K in units of J_{FM}. In this work, 10^4 MC steps per spin (MCSS) were used at each field step for the hysteresis loops, and the results were averaged over 60 different samples (namely, random numbers).

[1] C. Gleitzer and J. B. Goodenough, *Mixed-Valence Iron Oxides*, in *Cation Ordering and Electron Transfer. Structure and Bonding*, Vol. 61 (Springer, Berlin, Heidelberg, 1985), pp. 1–76.

[2] P. Tartaj, M. P. Morales, T. Gonzalez-Carreño, S. Veintemillas-Verdaguer, and C. J. Serna, *The Iron Oxides Strike Back: From Biomedical Applications to Energy Storage Devices and Photoelectrochemical Water Splitting*, Adv. Mater. **23**, 5243 (2011).

[3] E. A. Dobisz, Z. Z. Bandic, T. W. Wu, and T. Albrecht, *Patterned Media: Nanofabrication Challenges of Future Disk Drives*, Proc. IEEE **96**, 1836 (2008).

[4] Q. A. Pankhurst, J. Connolly, S. K. Jones, and J. Dobson, *Applications of Magnetic Nanoparticles in Biomedicine*, J. Phys. D **36**, R167 (2003).

[5] G. C. Papaefthymiou, *Nanoparticle Magnetism*, Nano Today **4**, 438 (2009).

[6] D. Yoo, J.-H. Lee, T.-H. Shin, and J. Cheon, *Theranostic Magnetic Nanoparticles*, Acc. Chem. Res. **44**, 863 (2011).

[7] D. Yoo, H. Jeong, S.-H. Noh, J.-H. Lee, and J. Cheon, *Magnetically Triggered Dual Functional Nanoparticles for Resistance-Free Apoptotic Hyperthermia*, Angew. Chem., Int. Ed. Engl. **52**, 13047 (2013).

[8] R. E. Rosensweig, *Heating Magnetic Fluid with Alternating Magnetic Field*, J. Magn. Magn. Mater. **252**, 370 (2002).

[9] J.-P. Fortin, C. Wilhelm, J. Servais, C. Ménager, J.-C. Bacri, and F. Gazeau, *Size-Sorted Anionic Iron Oxide Nanomagnets as Colloidal Mediators for Magnetic Hyperthermia*, J. Am. Chem. Soc. **129**, 2628 (2007).

[10] S. Noh, W. Na, J. Jang, J.-H. Lee, E. J. Lee, S. H. Moon, Y. Lim, J.-S. Shin, and J. Cheon, *Nanoscale Magnetism Control via Surface and Exchange Anisotropy for Optimized Ferrimagnetic Hysteresis*, Nano Lett. **12**, 3716 (2012).

[11] A. H. Habib, C. L. Ondeck, P. Chaudhary, M. R. Bockstaller, and M. E. McHenry, *Evaluation of Iron-Cobalt/Ferrite Core-Shell Nanoparticles for Cancer Thermotherapy*, J. Appl. Phys. **103,** 07A307 (2008).

[12] A. Meffre, B. Mehdaoui, V. Kelsen, P. F. Fazzini, J. Carrey, S. Lachaize, M. Respaud, and B. Chaudret, *A Simple Chemical Route toward Monodisperse Iron Carbide Nanoparticles Displaying Tunable Magnetic and Unprecedented Hyperthermia Properties*, Nano Lett. **12,** 4722 (2012).

[13] J. Kolosnjaj-Tabi, L. Lartigue, Y. Javed, N. Luciani, T. Pellegrino, C. Wilhelm, D. Alloyeau, and F. Gazeau, *Biotransformations of Magnetic Nanoparticles in the Body*, Nano Today **11,** 280 (2016).

[14] J.-H. Lee, J. Jang, J. Choi, S. H. Moon, S. Noh, J. Kim, J.-G. Kim, I.-S. Kim, K. I. Park, and J. Cheon, *Exchange-Coupled Magnetic Nanoparticles for Efficient Heat Induction*, Nat. Nanotechnol. **6,** 418 (2011).

[15] A. López-Ortega, M. Estrader, G. Salazar-Alvarez, A. G. Roca, and J. Nogués, *Applications of Exchange Coupled Bi-magnetic Hard/Soft and Soft/Hard Magnetic Core/Shell Nanoparticles*, Phys. Rep. **553,** 1 (2015).

[16] J. Nogués and I. K. Schuller, *Exchange Bias*, J. Magn. Magn. Mater. **192,** 203 (1999).

[17] M. Vasilakaki, C. Binns, and K. N. Trohidou, *Susceptibility Losses in Heating of Magnetic Core/Shell Nanoparticles for Hyperthermia: A Monte Carlo Study of Shape and Size Effects*, Nanoscale **7,** 7753 (2015).

[18] J. Park, K. An, Y. Hwang, J.-G. Park, H.-J. Noh, J.-Y. Kim, J.-H. Park, N.-M. Hwang, and T. Hyeon, *Ultra-Large-Scale Syntheses of Monodisperse Nanocrystals*, Nat. Mater. **3,** 891 (2004).

[19] L. Qiao, Z. Fu, J. Li, J. Ghosen, M. Zeng, J. Stebbins, P. N. Prasad, and M. T. Swihart, *Standardizing Size- and Shape-Controlled Synthesis of Monodisperse Magnetite (Fe$_3$O$_4$) Nanocrystals by Identifying and Exploiting Effects of Organic Impurities*, ACS Nano **11,** 6370 (2017).

[20] A. Kostopoulou, F. Thétiot, I. Tsiaoussis, M. Androulidaki, P. D. Cozzoli, and A. Lappas, *Colloidal Anisotropic* ZnO − Fe@Fe$_x$O$_y$ *Nanoarchitectures with Interface-Mediated Exchange-Bias and Band-Edge Ultraviolet Fluorescence*, Chem. Mater. **24,** 2722 (2012).

[21] E. Lima, E. L. Winkler, D. Tobia, H. E. Troiani, R. D. Zysler, E. Agostinelli, and D. Fiorani, *Bimagnetic* CoO *Core*/CoFe$_2$O$_4$ *Shell Nanoparticles: Synthesis and Magnetic Properties*, Chem. Mater. **24,** 512 (2012).

[22] H. Zeng, S. Sun, J. Li, Z. L. Wang, and J. P. Liu, *Tailoring Magnetic Properties of Core/Shell Nanoparticles*, Appl. Phys. Lett. **85,** 792 (2004).

[23] F. X. Redl, C. T. Black, G. C. Papaefthymiou, R. L. Sandstrom, M. Yin, H. Zeng, C. B. Murray, and S. P. O'Brien, *Magnetic, Electronic, and Structural Characterization of Nonstoichiometric Iron Oxides at the Nanoscale*, J. Am. Chem. Soc. **126,** 14583 (2004).

[24] M. Levy, A. Quarta, A. Espinosa, A. Figuerola, C. Wilhelm, M. García-Hernández, A. Genovese, A. Falqui, D. Alloyeau, R. Buonsanti *et al.*, *Correlating Magneto-Structural Properties to Hyperthermia Performance of Highly Monodisperse Iron Oxide Nanoparticles Prepared by a Seeded-Growth Route*, Chem. Mater. **23,** 4170 (2011).

[25] E. Wetterskog, C.-W. Tai, J. Grins, L. Bergström, and G. Salazar-Alvarez, *Anomalous Magnetic Properties of Nanoparticles Arising from Defect Structures: Topotaxial Oxidation of* Fe$_{1-x}$O/Fe$_{3-\delta}$O$_4$ *Core/Shell Nanocubes to Single-Phase Particles*, ACS Nano **7,** 7132 (2013).

[26] A. Walter, C. Billotey, A. Garofalo, C. Ulhaq-Bouillet, C. Lefèvre, J. Taleb, S. Laurent, L. V. Elst, R. N. Muller, L. Lartigue *et al.*, *Mastering the Shape and Composition of Dendronized Iron Oxide Nanoparticles To Tailor Magnetic Resonance Imaging and Hyperthermia*, Chem. Mater. **26,** 5252 (2014).

[27] C. A. McCammon and L. Liu, *The Effects of Pressure and Temperature on Nonstoichiometric Wüstite,* Fe$_x$O: *The Iron-Rich Phase Boundary*, Phys. Chem. Miner. **10,** 106 (1984).

[28] C. R. A. Catlow and B. E. F. Fender, *Calculations of Defect Clustering in* Fe$_{1-x}$O, J. Phys. C Solid State Phys. **8,** 3267 (1975).

[29] B. P. Pichon, O. Gerber, C. Lefevre, I. Florea, S. Fleutot, W. Baaziz, M. Pauly, M. Ohlmann, C. Ulhaq, O. Ersen *et al.*, *Microstructural and Magnetic Investigations of Wüstite-Spinel Core-Shell Cubic-Shaped Nanoparticles*, Chem. Mater. **23,** 2886 (2011).

[30] X. Sun, N. F. Huls, A. Sigdel, and S. Sun, *Tuning Exchange Bias in Core/Shell* FeO/Fe$_3$O$_4$ *Nanoparticles*, Nano Lett. **12,** 246 (2012).

[31] D. T. Margulies, F. T. Parker, M. L. Rudee, F. E. Spada, J. N. Chapman, P. R. Aitchison, and A. E. Berkowitz, *Origin of the Anomalous Magnetic Behavior in Single Crystal* Fe$_3$O$_4$ *Films*, Phys. Rev. Lett. **79,** 5162 (1997).

[32] K. P. McKenna, F. Hofer, D. Gilks, V. K. Lazarov, C. Chen, Z. Wang, and Y. Ikuhara, *Atomic-Scale Structure and Properties of Highly Stable Antiphase Boundary Defects in* Fe$_3$O$_4$, Nat. Commun. **5,** 5740 (2014).

[33] Z. Nedelkoski, D. Kepaptsoglou, L. Lari, T. Wen, R. A. Booth, S. D. Oberdick, P. L. Galindo, Q. M. Ramasse, R. F. L. Evans, S. Majetich *et al.*, *Origin of Reduced Magnetization and Domain Formation in Small Magnetite Nanoparticles*, Sci. Rep. **7,** 45997 (2017).

[34] R. Chen, M. G. Christiansen, A. Sourakov, A. Mohr, Y. Matsumoto, S. Okada, A. Jasanoff, and P. Anikeeva, *High-Performance Ferrite Nanoparticles through Nonaqueous Redox Phase Tuning*, Nano Lett. **16,** 1345 (2016).

[35] H. Khurshid, W. Li, S. Chandra, M.-H. Phan, G. C. Hadjipanayis, P. Mukherjee, and H. Srikanth, *Mechanism and Controlled Growth of Shape and Size Variant Core/Shell* FeO/Fe$_3$O$_4$ *Nanoparticles*, Nanoscale **5,** 7942 (2013).

[36] M. Estrader, A. López-Ortega, I. V. Golosovsky, S. Estradé, A. G. Roca, G. Salazar-Alvarez, L. López-Conesa, D. Tobia, E. Winkler, J. D. Ardisson *et al.*, *Origin of the Large Dispersion of Magnetic Properties in Nanostructured Oxides:* Fe$_x$O/Fe$_3$O$_4$ *Nanoparticles as a Case Study*, Nanoscale **7,** 3002 (2015).

[37] P. Tancredi, P. C. R. Rojas, O. Moscoso-Londoño, U. Wolff, V. Neu, C. Damm, B. Rellinghaus, M. Knobel, and L. M. Socolovsky, *Synthesis Process, Size and Composition Effects of Spherical* Fe$_3$O$_4$ *and* FeO@Fe$_3$O$_4$ *Core/Shell Nanoparticles*, New J. Chem. **41,** 15033 (2017).

[38] S. J. L. Billinge and I. Levin, *The Problem with Determining Atomic Structure at the Nanoscale*, Science **316**, 561 (2007).

[39] T. Egami and S. J. L. Billinge, *Underneath the Bragg Peaks: Structural Analysis of Complex Materials* (Elsevier, Oxford, UK, 2003), 1 st ed., Vol. 7.

[40] G. Vallejo-Fernandez, O. Whear, A. G. Roca, S. Hussain, J. Timmis, V. Patel, and K. O'Grady, *Mechanisms of Hyperthermia in Magnetic Nanoparticles*, J. Phys. D **46**, 312001 (2013).

[41] R. Hergt, S. Dutz, and M. Zeisberger, *Validity Limits of the Néel Relaxation Model of Magnetic Nanoparticles for Hyperthermia*, Nanotechnology **21**, 015706 (2010).

[42] R. M. Hazen and R. Jeanloz, *Wüstite (*Fe$_{1-x}$O*): A Review of Its Defect Structure and Physical Properties*, Rev. Geophys. **22**, 37 (1984).

[43] M. J. Hÿtch, J.-L. Putaux, and J.-M. Pénisson, *Measurement of the Displacement Field of Dislocations to 0.03 Å by Electron Microscopy*, Nature (London) **423**, 270 (2003).

[44] See Supplemental Material at http://link.aps.org/supplemental/10.1103/PhysRevX.9.041044 for detailed comparison of different size and shape nanocrystals, including refinement of their structural parameters, together with experimental data and theoretical results quantifying their nanomagnetism.

[45] W. H. Bragg, *XXX. The Structure of the Spinel Group of Crystals*, Lond. Edinb. Dublin Philos. Mag. J. Sci. **30**, 305 (1915).

[46] M. S. Senn, J. P. Wright, and J. P. Attfield, *Charge Order and Three-Site Distortions in the Verwey Structure of Magnetite*, Nature (London) **481**, 173 (2012).

[47] G. Ferguson and M. Hass, *Magnetic Structure and Vacancy Distribution in γ-*Fe$_2$O$_3$ *by Neutron Diffraction*, Phys. Rev. **112**, 1130 (1958).

[48] R. J. Armstrong, A. H. Morrish, and G. A. Sawatzky, *Mössbauer Study of Ferric Ions in the Tetrahedral and Octahedral Sites of a Spinel*, Phys. Lett. **23**, 414 (1966).

[49] A. Tomas, P. Laruelle, J. L. Dormann, and M. Nogues, *Affinement de la structure des formes ordonnée et désordonnée de l'octaoxopentaferrate de lithium,* LiFe$_5$O$_8$, Acta Crystallogr. C **39**, 1615 (1983).

[50] S. J. Marin, M. O'Keeffe, and D. E. Partin, *Structures and Crystal Chemistry of Ordered Spinels:* LiFe$_5$O$_8$, LiZnNbO$_4$, *and* Zn$_2$TiO$_4$, J. Solid State Chem. **113**, 413 (1994).

[51] G. W. Van Oosterhout and C. J. M. Rooijmans, *A New Superstructure in Gamma-Ferric Oxide*, Nature (London) **181**, 44 (1958).

[52] C. Greaves, *A Powder Neutron Diffraction Investigation of Vacancy Ordering and Covalence in γ-*Fe$_2$O$_3$, J. Solid State Chem. **49**, 325 (1983).

[53] S. Yang and X. Ren, *Noncubic Crystallographic Symmetry of a Cubic Ferromagnet: Simultaneous Sructural Change at the Ferromagnetic Transition*, Phys. Rev. B **77**, 014407 (2008).

[54] H. Y. Huang, Z. Y. Chen, R.-P. Wang, F. M. F. de Groot, W. B. Wu, J. Okamoto, A. Chainani, A. Singh, Z.-Y. Li, J.-S. Zhou *et al.*, *Jahn-Teller Distortion Driven Magnetic Polarons in Magnetite*, Nat. Commun. **8**, 15929 (2017).

[55] B. Antic, M. Perovic, A. Kremenovic, J. Blanusa, V. Spasojevic, P. Vulic, L. Bessais, and E. S. Bozin, *An Integrated Study of Thermal Treatment Effects on the Microstructure and Magnetic Properties of Zn–Ferrite Nanoparticles*, J. Phys. Condens. Matter **25**, 086001 (2013).

[56] V. Petkov, P. D. Cozzoli, R. Buonsanti, R. Cingolani, and Y. Ren, *Size, Shape, and Internal Atomic Ordering of Nanocrystals by Atomic Pair Distribution Functions: A Comparative Study of γ-*Fe$_2$O$_3$ *Nanosized Spheres and Tetrapods*, J. Am. Chem. Soc. **131**, 14264 (2009).

[57] F. Walz, *The Verwey Transition—A Topical Review*, J. Phys. Condens. Matter **14**, R285 (2002).

[58] A. P. Roberts, Y. Cui, and K. L. Verosub, *Wasp-Waisted Hysteresis Loops: Mineral Magnetic Characteristics and Discrimination of Components in Mixed Magnetic Systems*, J. Geophys. Res. Solid Earth **100**, 17909 (1995).

[59] Q. Song and Z. J. Zhang, *Controlled Synthesis and Magnetic Properties of Bimagnetic Spinel Ferrite* CoFe$_2$O$_4$ *and* MnFe$_2$O$_4$ *Nanocrystals with Core–Shell Architecture*, J. Am. Chem. Soc. **134**, 10182 (2012).

[60] M. Vasilakaki and K. N. Trohidou, *Numerical Study of the Exchange-Bias Effect in Nanoparticles with Ferromagnetic Core/Ferrimagnetic Disordered Shell Morphology*, Phys. Rev. B **79**, 144402 (2009).

[61] M. Vasilakaki, K. N. Trohidou, and J. Nogués, *Enhanced Magnetic Properties in Antiferromagnetic-Core/Ferrimagnetic-Shell Nanoparticles*, Sci. Rep. **5**, 9609 (2015).

[62] P. J. Saines, M. G. Tucker, D. A. Keen, A. K. Cheetham, and A. L. Goodwin, *Coupling of the Local Defect and Magnetic Structure of Wüstite* Fe$_{1-x}$O, Phys. Rev. B **88**, 134418 (2013).

[63] T. R. Welberry, D. J. Goossens, and A. P. Heerdegen, *Local Order in Wüstite Using a Pair Distribution Function (PDF) Approach*, Mineral Mag. **78**, 373 (2014).

[64] E. E. Fullerton, J. S. Jiang, and S. D. Bader, *Hard/Soft Magnetic Heterostructures: Model Exchange-Spring Magnets*, J. Magn. Magn. Mater. **200**, 392 (1999).

[65] S. K. Arora, R. G. S. Sofin, A. Nolan, and I. V. Shvets, *Antiphase Boundaries Induced Exchange Coupling in Epitaxial* Fe$_3$O$_4$ *Thin Films*, J. Magn. Magn. Mater. **286**, 463 (2005).

[66] M. P. Morales, S. Veintemillas-Verdaguer, M. I. Montero, C. J. Serna, A. Roig, L. Casas, B. Martínez, and F. Sandiumenge, *Surface and Internal Spin Canting in* γ − Fe$_2$O$_3$ *Nanoparticles*, Chem. Mater. **11**, 3058 (1999).

[67] M. S. Carrião and A. F. Bakuzis, *Mean-Field and Linear Regime Approach to Magnetic Hyperthermia of Core–Shell Nanoparticles: Can Tiny Nanostructures Fight Cancer?*, Nanoscale **8**, 8363 (2016).

[68] C.-J. Chen, R.-K. Chiang, H.-Y. Lai, and C.-R. Lin, *Characterization of Monodisperse Wüstite Nanoparticles Following Partial Oxidation*, J. Phys. Chem. C **114**, 4258 (2010).

[69] D. W. Kavich, J. H. Dickerson, S. V. Mahajan, S. A. Hasan, and J.-H. Park, *Exchange Bias of Singly Inverted* FeO/Fe$_3$O$_4$ *Core-Shell Nanocrystals*, Phys. Rev. B **78**, 174414 (2008).

[70] L. M. Bronstein, X. Huang, J. Retrum, A. Schmucker, M. Pink, B. D. Stein, and B. Dragnea, *Influence of Iron Oleate*

Complex Structure on Iron Oxide Nanoparticle Formation, Chem. Mater. **19**, 3624 (2007).

[71] M. I. Bodnarchuk, M. V. Kovalenko, H. Groiss, R. Resel, M. Reissner, G. Hesser, R. T. Lechner, W. Steiner, F. Schäffler, and W. Heiss, *Exchange-Coupled Bimagnetic Wüstite/Metal Ferrite Core/Shell Nanocrystals: Size, Shape, and Compositional Control*, Small **5**, 2247 (2009).

[72] W. W. Yu, J. C. Falkner, C. T. Yavuz, and V. L. Colvin, *Synthesis of Monodisperse Iron Oxide Nanocrystals by Thermal Decomposition of Iron Carboxylate Salts*, Chem. Commun. **20**, 2306 (2004).

[73] C. A. Schneider, W. S. Rasband, and K. W. Eliceiri, *NIH Image to ImageJ: 25 Years of Image Analysis*, Nat. Methods **9**, 671 (2012).

[74] C. L. Farrow, P. Juhas, J. W. Liu, D. Bryndin, E. S. Božin, J. Bloch, T. Proffen, and S. J. L. Billinge, *PDFfit2 and PDFgui: Computer Programs for Studying Nanostructure in Crystals*, J. Phys. Condens. Matter **19**, 335219 (2007).

[75] F. Gazeau, J. C. Bacri, F. Gendron, R. Perzynski, Yu. L. Raikher, V. I. Stepanov, and E. Dubois, *Magnetic Resonance of Ferrite Nanoparticles: Evidence of Surface Effects*, J. Magn. Magn. Mater. **186**, 175 (1998).

[76] G. F. Goya, T. S. Berquó, F. C. Fonseca, and M. P. Morales, *Static and Dynamic Magnetic Properties of Spherical Magnetite Nanoparticles*, J. Appl. Phys. **94**, 3520 (2003).

[77] K. Binder and D. Heermann, *Monte Carlo Simulation in Statistical Physics: An Introduction*, 5th ed. (Springer-Verlag, Berlin, Heidelberg, 2010).